Hydrogen impurity in yttria: *Ab initio* and μSR perspectives

E. L. Silva* and A. G. Marinopoulos
Centro de Estudos de Materiais por Difracção de Raios-x (CEMDRX) and Center for Computational Physics, Department of Physics, University of Coimbra, P-3004-516 Coimbra, Portugal

R. C. Vilão, R. B. L. Vieira, H. V. Alberto, J. Piroto Duarte,† and J. M. Gil
Centro de Estudos de Materiais por Difracção de Raios-x (CEMDRX), Department of Physics, University of Coimbra, P-3004-516 Coimbra, Portugal

(Received 23 January 2012; published 27 April 2012)

The incorporation of interstitial hydrogen in yttria was studied by means of *ab initio* calculations based on density-functional theory (DFT) and muonium spin polarization spectroscopy (μSR). The density-functional calculations, based on a semilocal functional within the GGA-PBE and a hybrid functional, uncovered multiple geometrical configurations for the neutral, H^0, and the negatively charged, H^-, states of hydrogen, thus demonstrating the existence of metastable minimum-energy sites. It was observed that the low-energy configurations for H^0 and H^- are similar: they prefer to relax in deep, interstitial sites, whereas the equilibrium configurations for the positively charged state, H^+, were bond-type configurations with the hydrogen forming a covalent O-H bond with an O anion. For all neutral and negative configurations, localized defect levels were found inside the gap. Overall, the results for the formation energies obtained by the two different functionals are qualitatively similar; an amphoteric behavior was found for hydrogen after considering the lowest-energy structures for each charge state. The calculated acceptor transition level, obtained by the hybrid functional and seen near midgap, is consistent with μSR data from literature. The results are consistent with the present μSR data, where the observed diamagnetic signal is attributed to a donor-like muonium at the oxygen-bonded configurations and the paramagnetic signal to an acceptor-like deep muonium at the interstitial sites.

DOI: 10.1103/PhysRevB.85.165211 PACS number(s): 61.72.−y, 71.55.−i, 71.15.Nc, 76.75.+i

I. INTRODUCTION

Yttria (Y_2O_3) is a transition-metal oxide of the sesquioxide family, with a wide range of applications in ceramic materials' processing and as a host material for rare-earth-doped lasers.[1,2] It is also a candidate high dielectric constant (high-κ) oxide to replace SiO_2 as the gate dielectric in metal-oxide-semiconductor devices.[3] High-κ oxides can serve as suitable replacements, since the thicker layer of the candidate oxide may exponentially decrease the tunneling currents arising from the reduction of the layer thickness of the SiO_2 gate dielectric,[3] while achieving the same level of capacitance as the devices of SiO_2.[1] Y_2O_3 is being considered as a suitable candidate for this purpose as it possesses relatively high dielectric constant ($\sim$15)[3] and acts as an insulator with a 6-eV gap width,[3] which enables band offsets with respect to the adjoining Si semiconductor of over 1 eV, thus minimizing carrier injection into its bands by acting as barriers of potential.[3–5] This oxide is also thermodynamically stable in contact with Si, inhibiting the formation of thin insulating layers at the interface.[3] Y_2O_3 is one of the few oxides epitaxially matched with the silicon lattice, therefore enabling a potentially low density of interface defects,[2,3] mainly attributed to oxygen related defects[6] that are responsible for device degradation due to trap carriers, threshold voltage instability and charge scattering in the semiconductor channel.[2,3,7]

Considerable effort has been directed toward the study of defects in semiconductors and insulators and how these can affect device properties and reliability.[3,7] The interstitial hydrogen is most prominent among such defects, since it can be unintentionally incorporated during the growth or the processing of the material.[8] It is well known that interstitial hydrogen exhibits complex behaviors when introduced in materials.[9] Hydrogen can interact with other dopants, as happens for example in Ge, where hydrogen is found to counteract electrical defects and activate neutral impurities.[10] Hydrogen is also used to passivate the dangling bonds at the SiO_2/Si interface.[11] In many other materials (as happens for example in GaN, where H^0 is never the lowest-energy state and a negative-U system is obtained) hydrogen acts as a deep, amphoteric impurity, which always counteracts the prevailing conductivity.[12] Hydrogen can also behave as a donor dopant, for instance in ZnO,[8,12,13] enabling a shallow defect level close to the conduction band. These findings motivate the research of the hydrogen behavior in other semiconductors and oxides, where it can influence the electrical properties.[8]

The dominant native ionic defects in Y_2O_3 are O interstitials and vacancies and it has been observed that undoped Y_2O_3 is a p conductor at high O_2 pressure.[14,15] The p conductivity usually decreases when the H_2O pressure increases, going from electronic to an ionic conductor due to the compensation of positively charged hydrogen impurities, mainly occurring as interstitial protons and/or hydroxide ions.[14,15] Therefore, when samples are exposed to hydrogen-containing gas and/or high water-vapor pressures, at low temperatures, hydrogen impurities have to be taken into account,[14,15] for these will dominate the ionic conductivity.[14,15]

Since hydrogen defects are very difficult to study experimentally, because hydrogen possesses high mobility and tends to pair with other defects,[16] μSR spectroscopy has become the standard technique to study isolated hydrogen in materials.[8,9,13,17] This technique exploits the rotation, relaxation and resonance of the spin of implanted muons and uses muonium, an electron bound to a positive muon, as a

pseudoisotope of hydrogen.[18,19] The short lifetime (2.2 μs) of the implanted positive muonium is reflected on the short time-scale measurements performed under nonequilibrium conditions and allows the observation of the isolated defect centers that are responsible for the electrical activity of hydrogen.[17,20,21] Although the muon is only one ninth the mass of the proton, the reduced mass of muonium is 99.6% of that of hydrogen, so that the respective electronic properties are basically the same in both atoms.[20] μSR spectroscopy has also the advantage of being sensitive to both neutral (paramagnetic) and charged (electronically diamagnetic) states of muonium and of being able to distinguish deep[22] and shallow centers.[16,23] Thus, extensive studies have already been carried out to verify whether deep muonium (resembling the atom-like localized state of hydrogen) or shallow-donor muonium are formed in different semiconductors and oxides, hence providing a reasonably good comparison to whether hydrogen behaves as a deep or shallow impurity, respectively.[17,18,22–26] Among these materials is Y_2O_3 where Cox *et al.*[18] have predicted the coexistence of deep muonium with the extended orbitals of a shallow-donor state. It was suggested from indirect evidence that the two states coexist at low temperatures and that deep muonium can also persist above room temperatures, enabling an acceptor level near midgap at 2.5 ± 1.5 eV[18] above the valence-band maximum (VBM).

The present *ab initio* study was focused on density-functional theory (DFT) calculations by employing both semilocal and hybrid nonlocal functionals, for hydrogen in the Y_2O_3 lattice. We determined the minimum-energy sites of the hydrogen impurity for all its different charge states (H^+, H^-, and H^0). Our aim was to obtain not only the lowest-energy configurations of hydrogen but also higher-energy metastable structures with different geometrical configurations. The formation energies were also calculated to study the behavior that hydrogen exhibits in Y_2O_3 for the different geometrical configurations in order to compare to nonequilibrium μSR measurements that can access these higher-energy states. The position of the defect energy levels in the band gap were also evaluated, as well as the charge isosurfaces of the neutral paramagnetic systems in order to provide a more detailed information regarding the nature and localization of the impurity states.

Due to the highly reasonable description of the structural parameters with respect to experimental data and to smaller computational cost, *ab initio* calculations in solids are generally carried out by applying local and semilocal functionals of the exchange and correlation, although it is well known that these type of functionals provide poor accuracy of the energy band gaps of materials.[27,28] Therefore, new levels of theory are needed in order to overcome these uncertainties and hence attain more accurate results. For solid-state systems, the hybrid screened Heyd-Scuseria-Ernzerhof (HSE)[29] functional proved to give very good results for oxides, where the structural parameters result in better agreement with experiment than the results evaluated by employing the local density approximation (LDA) and the gradient generalized approximation (GGA) functionals.[27,30–37] Calculations based on this level of theory for the hydrogen impurity in Y_2O_3 are lacking and as such the present work provides accurate theoretical results to compare with the μSR data.

In the μSR experiments reported here, positive muons were implanted in a polycrystalline Y_2O_3 sample and conventional transverse-field measurements[19] were undertaken from liquid-helium temperature up to room temperature. We were able to follow directly the deep muonium state with high-resolution measurements at the Paul Scherrer Institut in Switzerland. The discussion of results is intended to be developed taking into account the comparison between the theoretical and the experimental data.

In Sec. II the theoretical and experimental methodologies are introduced. In Sec. II A, the description of the theoretical framework, including the requirements for the numerical accuracy of the calculations and the formation energies of interstitial hydrogen are included. In Sec. II B the conditions and settings of the μSR measurements and apparatus are described. In Sec. III the results from theory and experiment are presented in detail and comparisons are made between similarities encountered throughout the work.

II. THEORETICAL AND EXPERIMENTAL METHODOLOGIES

A. Theoretical method and bulk-crystal calculations

The Y_2O_3 unit cell consists of a 40-atom body-centered cubic structure,[38] belonging to the space group Ia3-(Th7) (No. 206). The conventional cell can also be represented as an 80-atom cubic c-type structure[39–41] (see Fig. 1). It is formed by 64 slightly distorted minicubes composed of O anions; only 32 centers of these minicubes are occupied by Y cations

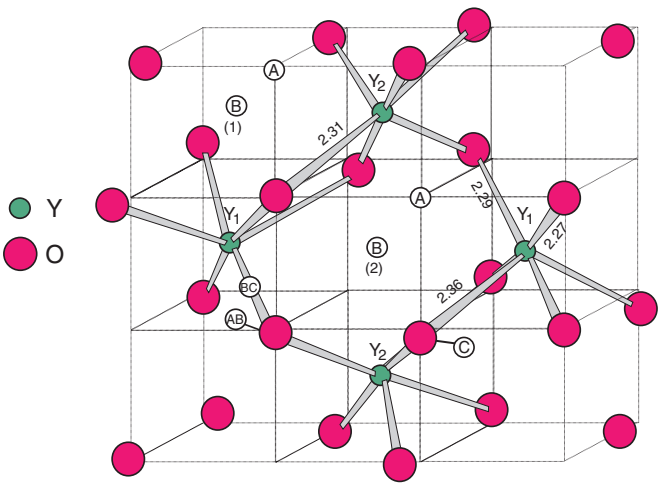

FIG. 1. (Color online) Part of the Y_2O_3 unit cell: O is represented by the pink balls and Y by the green balls. The different sites where hydrogen can be placed in the lattice are represented by the respective symbols. Type-A and Type-B [with two different surrounding environments, B(1) and B(2)] are interstitial sites, the Type-C site (C) refers to a bond O-H configuration (only one O-H configuration is depicted, although there are more with different environments). BC is the bond-center site and AB_O the antibonding O configuration (where the AB_Y is similar, but related to a Y cation). The values refer to the distances between the Y center and the respective surrounding anions and are represented in angstroms.

TABLE I. Values of the internal parameters, lattice constant, bulk modulus, and energy band gap obtained from the GGA-PBE and HSE06 present calculations for the Y_2O_3 lattice and compared with other theoretical and experimental data.

	u	x	y	z	a_0 (Å)	B (GPa)	E_{gap} (eV)
GGA-PBE (PAW)[a]	–0.0326	0.3913	0.1519	0.3795	10.706	136.111	4.13
HSE06 (PAW)[a]	–0.0326	0.3914	0.1518	0.3795	10.623	151.238	5.95
LDA (PAW)[53]	–0.0326	0.3907	0.1514	0.3797	10.515	–	4.00
GGA (PAW)[53]	–0.0327	0.3908	0.1516	0.3799	10.700	–	4.00
GGA-PW92 (PAW)[2]	–0.0324	0.3908	0.1515	0.3798	10.700	150.000	4.10
Exp.[4,38,50]	–0.0314	0.3890	0.1500	0.3770	10.604	150.000	6.00

[a]Present calculations.

(the centers of the empty minicubes are structural vacant Y sites, denoted as Type-B sites). The structure has two different cation sites, Y_1 and Y_2; Y_1 is at the 8*b* site and Y_2 at the 24*d* site (see Fig. 1). The anions are at the 48*e* sites. Only six anions occupy eight of the corners of the minicubes, enabling an octahedral coordination for the cations.[2,39,42] The empty corners are therefore structural vacant O sites and are denoted as Type-A sites.[2,39,42] For the Y_2-centered minicubes, three O ions are at one face of the cube, and the other three are at the opposite face, all of the six anions being equally distanced from the cation center. The Y_1-centered minicubes have four O ions at one face and the other two at the opposite face; the distance between the anions and the respective cation center occurs with three different paired distances (Fig. 1).[42]

In the present study, the DFT calculations were performed by employing the generalized gradient approximation (GGA) with the Perdew, Burke, and Enzerhof (PBE) parametrization[43] and the Heyd-Scuseria-Ernzerhof (HSE06)[29] hybrid functional. The two referenced functionals are implemented in the Vienna *Ab Initio* Simulation Package (VASP)[44–46] code, which performs electronic structure calculations by employing plane-wave basis sets to expand the Kohn-Sham wave functions, thus taking advantage of the periodicity of extended systems. In order to represent the valence and semicore states that enter the chemical binding of the system projector augmented wave (PAW) pseudopotentials[47,48] were used (Y configuration: $4s^2 4p^6 5s^2 4d^1$ and O configuration: $2s^2 2p^4$).

Within the HSE06 hybrid-functional scheme the resulting expression for the exchange and correlation energy is

$$E_{xc}^{HSE} = \alpha E_x^{HF,SR}(\mu) + (1-\alpha)E_x^{PBE,SR}(\mu) + E_x^{PBE,LR}(\mu) + E_c^{PBE} \quad (1)$$

where E_c^{PBE} is the PBE correlation energy and E_x^{PBE} the PBE exchange energy. Assuming a dependency on a screened Coulomb potential, SR and LR denote the short- and long-range exchange energies, respectively. μ is the screening parameter and is chosen to be 0.2 $Å^{-1}$ for the HSE06 functional.[27] α is the mixing fraction of the exact exchange and in the present study for yttria it was taken to be 30% in order to match the calculated band-gap energy [equal to 5.95 eV (see Fig. 2)] to the experimental value of ∼6 eV found by photoemission and internal photoemission spectroscopy.[4]

Convergence tests and full structural relaxations were carried out for the bulk Y_2O_3 lattice against different values of the plane-wave cutoff energy and the Brillouin zone (BZ) sampling, for the two functionals. Within GGA-PBE, when employing a plane-wave cutoff energy of 450 eV and an

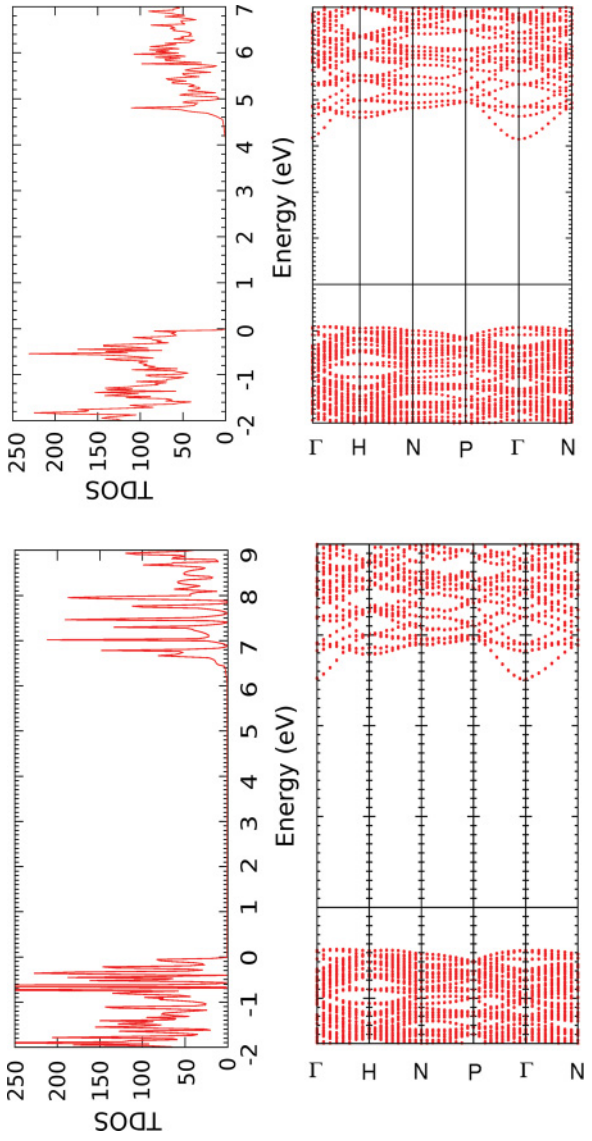

FIG. 2. (Color online) Band structure and density of states of Y_2O_3. The upper plot is evaluated using the GGA-PBE functional, where it can be observed that this structure has a direct energy gap of 4.13 eV. The lower plot refers to the HSE06 calculations where the increase of the gap width up to 5.95 eV is well noticed.

automatic mesh of $4 \times 4 \times 4$ Monkhorst-Pack grids[49] (to evaluate the total energies and the structural lattice relaxations) the lattice parameter of 10.706 Å was obtained, ∼1% higher than the experimental value of 10.604 Å.[50] Due to this increase we therefore observe an underestimation of the bulk modulus, with 136.111 ± 0.280 GPa obtained by using a Birch-Murningham equation of state fit, against the experimental value of 150 GPa[50] (deduced from compressive measurements on densified polycrystalline samples). The low value of the bulk modulus (theoretical and experimental) indicates the existence of soft bonds and, comparing to other results from GGA-PBE calculations performed on other sesquioxides, it is observed that these are of the same order of magnitude (127 GPa for La_2O_3,[51] 154 GPa for Lu_2O_3[52]). Results obtained from the present GGA-PBE calculations are summarized in Table I and are compared to other DFT results and experimental data for Y_2O_3.

To sample the BZ for the density of states (DOS), and therefore obtain a high-quality DOS, an automatic $6 \times 6 \times 6$ Γ-point-centered mesh was chosen for the GGA-PBE functional calculations.

To determine how the partial occupancies $f_{n\mathbf{k}}$ are set for each orbital, Gaussian smearing was applied, with the smearing width fixed at 0.2 eV. For the DOS calculations the tetrahedron method with Blöchl corrections was used, employing the same order of smearing width.

The obtained electronic band structure, total DOS, and site and angular momentum projected DOS are depicted in Figs. 2 and 3. Due to the underestimation of the band gap originated by employing the semilocal GGA-PBE functional, which does not take into account the derivative discontinuity in the exchange-correlation functional, we obtain a gap equal to 4.13 eV, a value that is consistent with earlier DFT-GGA calculations (see Table I).[2,53] From the band structure plot, Fig. 2, a direct band-gap structure is depicted, where the minimum of the conduction band and the maximum of the valence band are both centered at the Γ point. As for Fig. 3, the contributions from the different species that compose the lattice are well defined. The main contribution of the lowest-energy valence band (−21.3 eV to −20.8 eV) is due to the Y $4p$ states while the remaining two higher-energy valence bands are composed by the O states, the contribution of the highest-energy valence band (−3.9 eV to 0 eV) arising essentially from the $2p$ states. There is a small mixture of Y $4d$ states and O $2p$ states in the valence band, consistent with a limited covalent bonding between Y and O.[53] The cation-d nature of the conduction band (seen clearly in the DOS plots in Fig. 3) is a typical finding for transition-metal oxides.[53]

To perform HSE06 calculations and as these require a much more demanding computational effort, new convergence parameters for the plane-wave cutoff energy and for the BZ sampling had to be considered. Hence, the cutoff energy was reduced to 400 eV and an automatic mesh of $2 \times 2 \times 2$ Monkhorst-Pack grids[49] was applied for the structural energy calculations and a $2 \times 2 \times 2$ Γ-centered mesh for the DOS calculations.

The evaluated structural parameters and internal positions were in much better agreement with respect to the experimental values:[27] the respective lattice parameter resulted in 10.636 Å and the bulk modulus in 151.238 ± 3.061 GPa (fitted values by also using the Birch-Murningham equation of state) (see Table I).

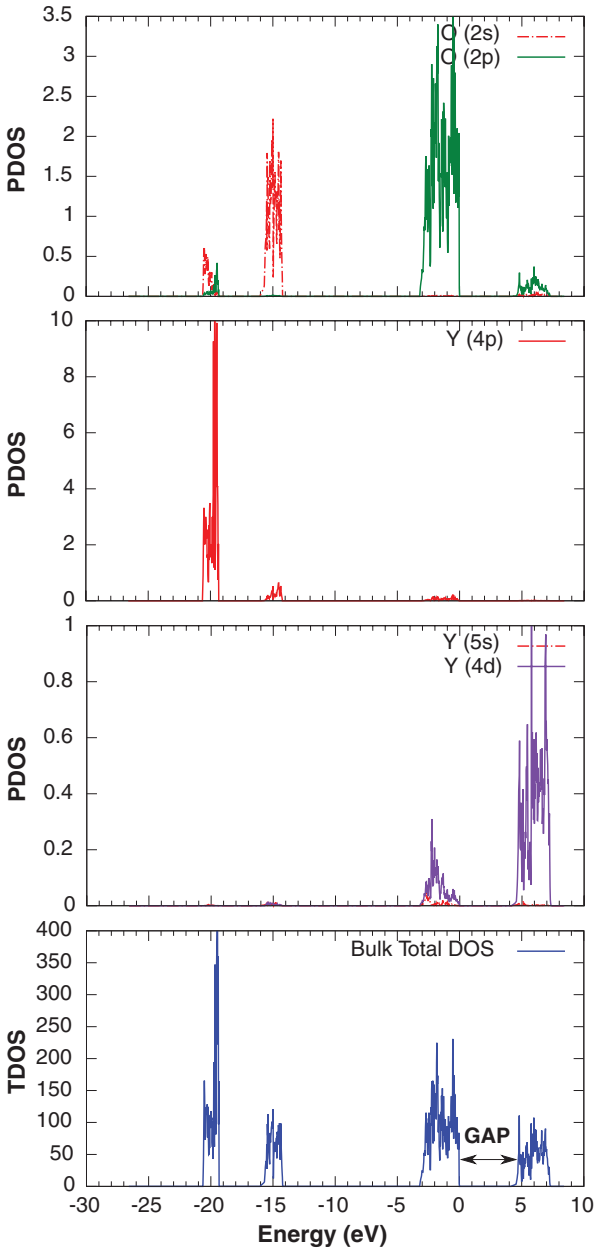

FIG. 3. (Color online) GGA-PBE density of states of the bulk Y_2O_3 lattice, where the angular-momentum (l) projected density of states of the O (first plot) and Y (second and third plot) ions and the total density of states have been plotted. The l-projected DOS has been evaluated by fixing the projecting radii to the respective ionic radii, with $r_Y = 0.93$ Å and $r_O = 1.40$ Å.

For the defect calculations, the 80-atom cubic structure is used as the supercell. The use of supercells is a natural choice in solid-state calculations, taking advantage of the periodicity of extended systems. Nevertheless one needs to take care when performing charged defect calculations.[28] The supercell method represents an infinite array of defects separated by lattice vectors and surrounded by the host species. When the lattice vectors are not large enough, spurious interactions

can take place from the nearby copies of the defect thus leading to systematic errors. In the case of charged defects, a neutralizing background charge had to be introduced in order to cancel electrostatic divergences. The electrostatic interaction between the defect cell and its periodic images can lead to slow convergence with respect to the supercell size.[28] Image corrections based on multipole expansion were thus added (up to the monopole-quadrupole interaction) to the total energies of the charged systems. The calculated corrections were found to be between the range of 0.13 eV to 0.15 eV, for the GGA-PBE and, for the hybrid calculations these were of the order of 0.10 eV to 0.14 eV.

The formation energies were evaluated in order to obtain the properties of hydrogen in the host material. The formation energy of interstitial hydrogen is defined as the energy needed to incorporate this impurity in the host lattice and is calculated by taking into account hydrogen in a charge state $q = \{-1, 0, +1\}$ by following the procedure from Refs. 9, 12, 54, and 55:

$$\mathrm{E_{form}}(\mathrm{H}^q) = \mathrm{E_{tot}}(\mathrm{H}^q) - \mathrm{E_{tot}}(\mathrm{bulk}) - \tfrac{1}{2}\mathrm{E_{tot}}(\mathrm{H_2}) + q(\mathrm{E_F} + E_{\mathrm{VBM}} + \Delta V). \quad (2)$$

$\mathrm{E_{tot}}(\mathrm{H}^q)$ is the total energy of the supercell with the hydrogen impurity of charge q, $\mathrm{E_{tot}}(\mathrm{bulk})$ is the total energy of the bulk supercell and $\frac{1}{2}\mathrm{E_{tot}}(\mathrm{H_2})$ is the reference energy for hydrogen that is given by an H_2 molecule at $T = 0$[54] (though this could be generalized by including a term for the chemical potential of hydrogen).[56] The Fermi level, $\mathrm{E_F}$, is referenced to the valence-band maximum of the bulk supercell, E_{VBM}. ΔV denotes a correction term that aligns the average electrostatic potential of the defect supercell with that in the bulk[55] (the change of the reference potential after introducing a defect).

B. Experimental details

The muon-spin rotation experiments took place at the EMU instrument of the ISIS Facility, Rutherford Appleton Laboratory, United Kingdom, and at the GPS instrument of the Muon Spin Laboratory at the Paul Scherrer Institut, Switzerland. In the experiments, a polycrystalline Y_2O_3 sample (obtained commercially from Alfa-Aesar) was used. Positive muons were implanted into the sample, and conventional transverse-field measurements[19] were undertaken from liquid-helium temperature up to room temperature. In Fig. 4 we present a muon spin rotation time spectrum obtained for a temperature $T = 275$ K and an external applied magnetic field of 1.5 mT. A clear diamagnetic line is observed, corresponding to an oscillation at the expected Larmor frequency of 200 kHz, which amounts to about 6% of the total muon spin polarization at this temperature. In the first 300 nanoseconds, as shown in the inset of Fig. 4 a clear muonium line is observed at the expected frequency of 21 MHz. This fast oscillation is seen to be superimposed to a highly relaxed component, and the fittings to these first channels do require the introduction of this third fast component, which does not correspond to any instrumental effect. As in Ref. 24, the question arises whether this fast component is either a heavily damped paramagnetic line or a diamagnetic component subject to lifetime broadening, the corresponding distinction not being possible to determine from the fits only. As will be discussed below, we assumed this fast component to be diamagnetic, and the analysis of the data was performed with the three components just described, by means of the function:

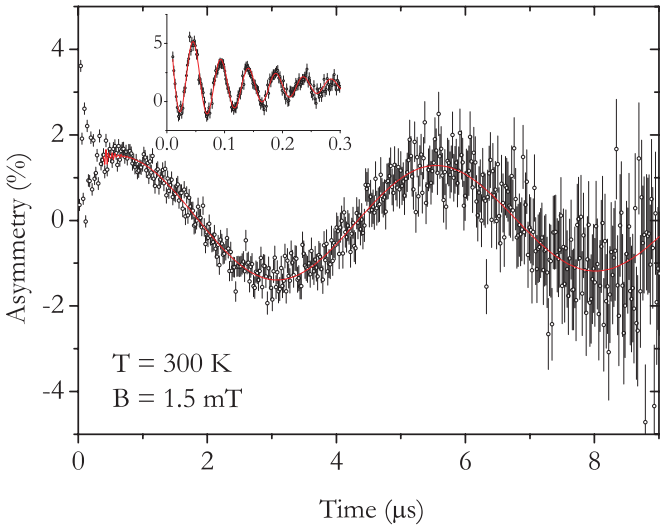

FIG. 4. (Color online) Muon spin asymmetry as a function of time, in transverse geometry (B = 1.5 mT), at $T = 300$ K (observed at PSI). A clear nearly undamped oscillation at the Larmor frequency is observed. In the first 300 nanoseconds, a relaxed 21 MHz muonium line is seen to oscillate around a strong relaxed decay (inset). Lines are fits as discussed in the text.

$$A(t) = [A_{\mathrm{slow}} \exp(-\lambda_{\mathrm{slow}} t) + A_{\mathrm{fast}} \exp(-\lambda_{\mathrm{fast}} t)] \cos(\omega_{\mathrm{d}} t + \phi_{\mathrm{d}}) + A_{\mathrm{Mu}} \exp(-\lambda_{\mathrm{Mu}} t) \cos(\omega_{\mathrm{Mu}} t + \phi_{\mathrm{Mu}}). \quad (3)$$

III. RESULTS AND DISCUSSION

A. Stable hydrogen configurations and formation energies

The study of hydrogen was performed by introducing the impurity in different sites in the lattice and with the three different charge states (H^+, H^-, and H^0). These sites include the already mentioned structural vacant O and Y sites (that we refer to as Type-A and Type-B sites, respectively), which are deep interstitial sites, the bond-type O-H sites (Type-C site), the O and Y antibonding sites (AB_O and AB_Y, respectively), and the bond-center site (BC) depicted in Fig. 1. This procedure allowed us to obtain not only the ground-state stable configurations of hydrogen but also the higher-energy metastable structures for each charge state.

Initial DFT calculations were carried out by employing the GGA-PBE functional, where all the structures were allowed to fully optimize. Taking the relaxed coordinates and for all minimum-energy configurations, calculations were repeated by employing the hybrid HSE06 functional, using a lower cutoff energy of 400 eV. The structures were allowed to relax for sufficient ionic steps in order to decrease the force between the ions.

Three different types of stable configurations were found for the neutral and negatively charged system and only one for the positively charged system, confirming therefore the

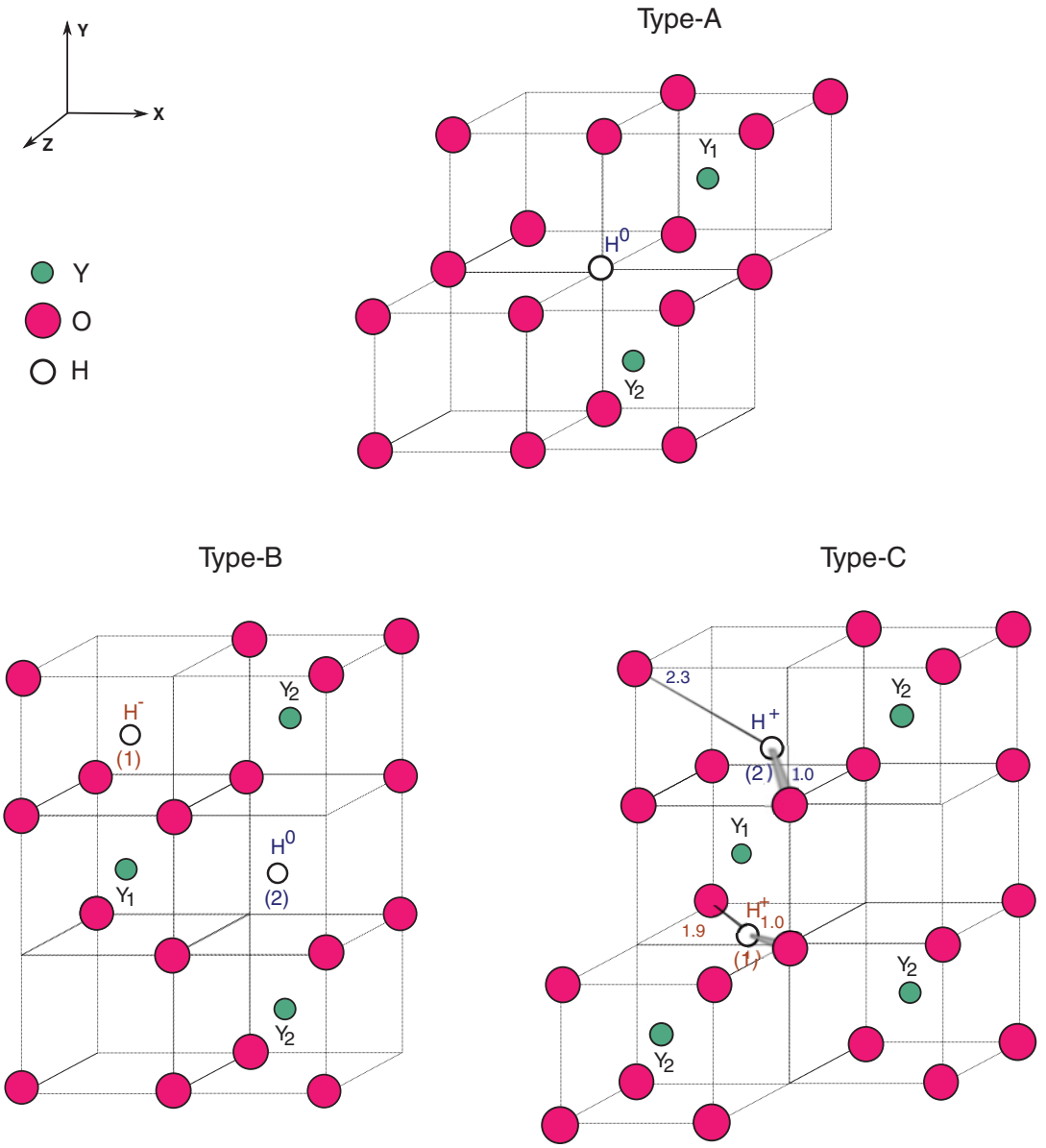

FIG. 5. (Color online) Representation of the hydrogen stable relaxed configurations for the three different charge states. The hydrogen is shown in white and by its charge states. For simplicity the Y_2O_3 lattice is represented by a perfect structure, where the distortion of the minicubes or the structural relaxations due to the incorporated impurity are not considered. Two different hydrogen positions appear for the Type-B configuration, Type-B(1) and Type-B(2), where the first position is assumed by the negatively charged and neutral system and the latter position only by the neutral system (the differences are due to the surrounding number of O ions). The Type-C configuration is found for the three charged states of hydrogen, and for the positively charged system this is the only stable configuration: the Type-C(1) is found to be the lowest-energy configuration, whereas the Type-C(2) is a higher-energy metastable configuration. The values refer to the distances between the hydrogen impurity with respect to the neighbor anions (GGA-PBE) and are represented in angstroms.

existence of multiple geometrical configurations with higher energies. In these stable configurations hydrogen occupied the Type-A, Type-B, and Type-C sites (see Figs. 1 and 5). The Type-C bond-type configuration was found to be the only stable configuration for the positively charged system. In contrast to what has been commonly found in covalent materials, the bond-center and antibonding sites are not stable sites for hydrogen in Y_2O_3. This suggests that this oxide has a sufficiently high degree of ionicity to destabilize these latter hydrogen configurations.

1. Positively charged systems (H^+)

The only type of stable configuration for the positively charged system occurs when the hydrogen impurity forms a strong covalent bond with an O anion, with a bond length of 1.00 Å. In this Type-C configuration, shown in Fig. 5, the impurity is strongly attracted by the anion and repelled by the nearest Y cation, hence displacing the O anion about 5% from its original position, placing it further away from the Y charge density. This bond-type configuration [Type-C(1) configuration] (see Fig. 5) is one of the different

bond-type configurations that may exist for the H^+ system. Two representative stable configurations are depicted in Fig. 5, where Type-C(1) stands for the lowest-energy configuration and Type-C(2) for the higher-energy configuration. The energy difference between these two systems is about 0.54 eV. The main reason for this energy difference resides in the next-neighbor positions: in the Type-C(1) site the H^+ is close to two O anions (at distances 1.00 Å and 1.88 Å) and to one Y cation (at 2.34 Å of distance) with the hydrogen impurity forming a bridge between the two O next neighbors. In the higher-energy configuration [Type-C(2)], H^+ has instead two close Y cation neighbors (at distances of 2.35 Å and 2.37 Å), one O anion forming a strong bond of 1.00 Å and the second nearest anion at 2.33 Å. This may explain why the energy of this latter system is higher: the two positively charged cations exert stronger repulsive forces to the positively charged impurity, therefore increasing the energy of this configuration.

Other higher-energy Type-C configurations were also obtained for the positively charged system, with formation energies strongly dependent on the local environment of the impurity. These differences reside specifically on the higher number of cation neighbors surrounding the hydrogen impurity, thus creating more instability upon the respective configuration.

2. *Neutral systems (H^0)*

For the neutral system, three different stable configurations exist. The lowest-energy configuration is obtained when hydrogen relaxes to a vacant O site, the Type-A configuration (see Fig. 5). Small structural relaxation occurs in the host lattice from the respective initial positions. The closest neighbors of the impurity are six O anions equally distanced at 2.5 Å away from hydrogen, and four Y cations at equally paired distances: two at 2.5 Å, and the other pair at 2.4 Å (depicted in Fig. 5).

Two other higher-energy configurations exist for the neutral system. One of them is the Type-C(1) configuration, where the impurity resides in the vicinity of a Y cation (at a distance of 2.38 Å) and two O anions: it forms a covalent O-H bond of 1.00 Å length with the closest anion and another longer bond of 1.98 Å with the second anion, similarly to what occurs for the positively charged system (see Fig. 5). The second metastable configuration that is observed for H^0 is the Type-B site, where the impurity relaxes to the center of a vacant minicube (depicted in Fig. 5). This vacant minicube corresponds to the Type-B(2) site, where the impurity is surrounded by six O anions (similarly to the Y_2 site for an occupied Y minicube, as discussed in Sec. II B). The relative energy differences between these two local minima with respect to the global minimum at the Type-A site is about 0.14 eV for the Type-C(1) and 0.17 eV for the Type-B(2) configuration.

The Type-B and the Type-C geometries assume two other distinct positions for this neutral charge state. For the Type-B structure, the second configuration differs from the one mentioned above because the hydrogen impurity is stabilized at the center of a Type-B(1) site minicube, represented in Fig. 5. The energy difference with respect to the lowest-energy structure is equal to 0.32 eV and from the Type-B(2) configuration is equal to 0.14 eV, thus possessing higher energy.

Similarly to the H^+ system, another higher-energy Type-C geometrical configuration exists with a different local environment, the Type-C(2) configuration. This structure differs from the Type-C(1) structure through the neighboring cations (see Fig. 5). Two Y cations are found to be close to the impurity, at a distance of 2.30 Å each, and a closest O anion is found to form a strong O-H bond of 1.00 Å of length. The second nearest O anion is 2.35 Å away from the impurity, at a longer distance than that found for the Type-C(1) structure [similarly to the metastable H^+ Type-C(2) structure of Fig. 5]. This higher-energy structure differs from the lowest-energy Type-A configuration by 0.29 eV and from the Type-C(1) system by 0.15 eV.

3. *Negatively charged systems (H^-)*

The H^- system also possesses three minimum-energy configurations, structurally similar to the neutral systems: the Type-A configuration has the lowest energy and the Type-B and Type-C geometry structures occur as higher-energy configurations. More specifically, the Type-B(1) structure occurs with considerably higher energy (1.24 eV) with respect to the lowest-energy Type-A structure (Fig. 5). The Type-B(2) structure was found to be unstable.

Similarly to the positively charged state, a variety of Type-C metastable configurations exist for the negative charge system: the Type-C(1) and the Type-C(2) configurations shown in Fig. 5 are among these. Nonetheless, they possess appreciably high formation energies: the former is 3.18 eV higher in energy when compared to the Type-A structure and the Type-C(2) has an even higher energy.

The relaxed configurations obtained by employing the HSE06 functional are very similar to the ones from GGA-PBE with some minor differences in the distances between the hydrogen and the neighboring ions. In terms of stability there is a difference in the energy ordering between the neutral configurations. From the GGA-PBE results the lowest-energy neutral configuration is obtained for hydrogen at the Type-A site (the other structures occur as high-energy metastable structures as already mentioned previously). With respect to the HSE06 calculations, however, the Type-C(1) configuration forms the lowest-energy configuration together with the Type-A configuration (the energy difference between these two configurations is only 0.02 eV).

Regarding the negatively charged systems, a slight increase in the energy difference between the lowest-energy structure and the two higher-energy metastable configurations, in comparison to the GGA-PBE calculations, is observed. The Type-B(1) structure differs energetically from the Type-A by 1.37 eV, the Type-C(1) by 3.51 eV, and the Type-C(2) by 4.47 eV.

From the GGA-PBE formation energies plotted in Fig. 6 (top) one can observe that hydrogen behaves as an amphoteric impurity when taking the lowest-energy configurations of the three different charge states into account. This behavior can be understood from the position of the charge transition levels, $E(q/q')$, inside the gap. These levels are defined as the Fermi-level positions for which the formation energies of the charge states q and q' are equal.[12] The donor level $E(+/0)$, the acceptor level $E(0/-)$ and the pinning level $E(+/-)$ thus

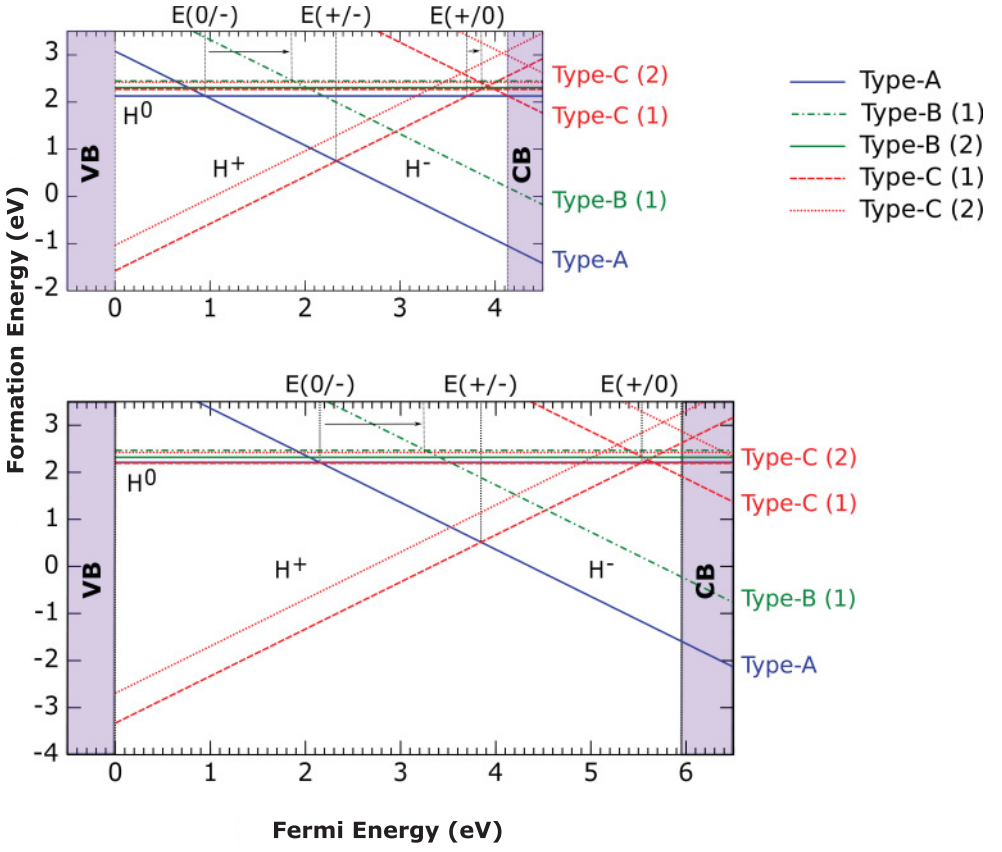

FIG. 6. (Color online) Formation energy of interstitial hydrogen as a function of the Fermi level in Y_2O_3 for multiple geometrical configurations. The range of E_F corresponds to the bulk theoretical band-gap with $E_F = 0$ at the VBM. The vertical lines are the donor level, $E(+/0)$, the acceptor level, $E(0/-)$, and the transition level, $E(+/-)$, of the lowest-energy structures. The arrows show the displaced transition levels when these are calculated for the higher-energy configurations (see text). The top plot corresponds to the GGA-PBE calculations whereas the bottom plot to the HSE06 calculations. The formation energies of the different geometrical configurations are represented by different line types and colors: the solid blue line represents the Type-A configuration, the dashed-dotted green line the Type-B(1) configuration, the solid green line the Type-B(2) configuration, the dashed red line the Type-C(1) configuration, and finally the dotted red line the Type-C(2) configuration.

govern the behavior of hydrogen. These levels are marked in Fig. 6 by the vertical lines. A negative-U behavior is seen to occur: there is a change in the respective energy ordering of the transition levels in the gap and the donor level, $E(+/0)$, lies above the acceptor level, $E(0/-)$. The pinning level $E(+/-)$ is found to be deep within the gap, at $E(+/-) = E_{\mathrm{VBM}} + 2.33$ eV from the GGA-PBE calculations. This means that the neutral state of hydrogen is never thermodynamically stable for any Fermi-level position within the gap. When the Fermi energy is below the $E(+/-)$ level we obtain a donor-like behavior for the impurity, thus enabling the compensation of acceptors in the host material. When the Fermi level is above the pinning level the opposite behavior is obtained, namely the compensation of donor dopants.[9,12] The donor level is positioned at $E(+/0) = E_{\mathrm{CBM}} - 0.4$ eV, not close enough to the CBM to induce n-type conductivity. Nevertheless, for hydrogen to act as a dopant, the pinning level would also have to be quite close to (or resonant with) the conduction-band minimum (CBM),[9] and this is not seen here. In an earlier first-principles GGA study[57,58] of the hydrogen impurity in Y_2O_3 it was concluded that hydrogen is a shallow donor and could be a possible source of positive fixed charge in the lattice.[57] It should nevertheless also be noted that these authors[57,58] used the high-temperature h phase of Y_2O_3 to perform the respective calculations.

Figure 6 displays the formation energies of higher-energy metastable configurations for each different charge state. This allows to define charge transition levels for each structural configuration that hydrogen (muonium) can adopt.[24] Such an assignment may in fact be more realistic especially when comparing theoretical predictions to experimental μSR data. Indeed, in μSR spectroscopy, due to the short lifetime of muonium ($2.2 \sim \mu$s), it is not possible to obtain full equilibrium measurements. Instead, higher-energy metastable states can also be accessed together with their acceptor and donor levels individually.

Examination of the new transition levels for the high-energy configurations shows important changes with respect to the equilibrium levels. In particular, the acceptor level, $E(0/-)$ for the higher-energy interstitial acceptor configuration, Type-B(1), becomes even deeper and is displaced toward midgap by about 0.9 eV (Fig. 6). This new position for $E(0/-)$ appears to be in better agreement with previous μSR data[18] for Y_2O_3. In that study deep muonium states were observed with a corresponding acceptor level near midgap at 2.5 ± 1.5 eV with respect to the valence-band maximum. Similar shifts

also occur for the transition levels of other configurations: the donor level of the bond-type C(1) configuration has an energy shift of 0.2 eV (Fig. 6) towards the CBM. For this Type-C(1) configuration the three transition levels are very close to each other. In fact there is an energy range where the neutral Type-C(1) configuration is stable (below the pinning level), hence indicating a positive-U ordering for hydrogen. The $E(+/-)$ and $E(+/0)$ levels are located 0.2 eV and 0.25 eV, respectively, below the CBM (depicted in Fig. 6, top plot), suggesting a donor behavior of hydrogen in this metastable geometric configuration. For the Type-C(2) configuration a positive-U ordering is also observed but the corresponding donor level lies further away from the CBM. From these results we infer that a portion of these bond-type configurations are donor-like configurations (Fig. 6) with corresponding donor and pinning levels very close to the CBM. Nevertheless, we cannot argue on the possibility of hydrogen behaving as a shallow donor due to the distance between the transition levels and the CBM.

The HSE06 results for the formation energies [Fig. 6 (bottom)] are similar to the GGA-PBE results. Again, an amphoteric behavior for hydrogen is obtained by considering the lowest-energy configurations for each charge state, with the pinning level $E(+/-)$ found in the upper half of the gap. Nonetheless, differences in the transition levels can easily be seen since these are shifted proportionally in the gap for the HSE06 framework: the $E(+/-)$ transition level of the lowest-energy configurations is pinned at 3.85 eV and the acceptor level $E(0/-)$ at 2.15 eV, above the valence-band maximum. The latter is consistent with the acceptor level that Cox and coworkers observed at 2.5 ± 1.5 eV (for deep muonium) through high-temperature μSR measurements performed above room temperature.[18]

Other differences between the GGA-PBE and HSE06 results also arise for the neutral system where a slight change of energy ordering between the different geometrical structures is observed (as already mentioned above). The neutral Type-C(1) configuration has now a lower energy, only by 0.02 eV with respect to the Type-A configuration, implying the existence of degenerate states.

Regarding the HSE06 formation energies and associated transition levels of the different geometrical configurations depicted in Fig. 6 (bottom), the results are also similar to the GGA-PBE results. The acceptor level corresponding to the interstitial Type-B(1) geometrical configuration is displaced to higher Fermi energies, 3.25 eV above the valence-band maximum, and is still in good agreement with the μSR data.[18] The donor level for the bond-type C(1) configuration is located 0.4 eV below the CBM, slightly deeper with respect to the GGA-PBE result. Similarly, the pinning level for Type-C(1) is also positioned 0.35 eV below the CBM, and a positive-U ordering can be observed with the neutral state being stable within a small-energy range.

B. Position of defect levels

In order to study the defect levels in the gap, the DOS of the different geometrical configurations were evaluated by applying the two mentioned functionals. For the neutral and negatively charged systems, a defect level in the gap is observed, whereas no defect level is observed for the positively charged systems. The position of the defect levels obtained by employing the two different functionals varies in proportion to the energy band gap (Fig. 7).

For the Type-A configuration, the defect level of the neutral system is positioned very close to the valence band, just 0.09 eV above the VBM (depicted in Fig. 7), for the GGA-PBE and HSE06 calculations. The defect levels of the Type-B(1) and Type-B(2) configurations are positioned slightly higher in the gap with respect to the lower-energy configuration levels: 1.00 eV and 0.50 eV above the VBM, respectively. For the HSE06 only the Type-B(2) configuration was calculated and the position of the defect level is observed to be 0.50 eV above the VBM. For the two Type-C configurations discussed in the preceding subsection, the defect-level positions differ from the former two levels. When employing the GGA-PBE functional, the defect level of the Type-C(1) configuration is observed to be 0.66 eV below the CBM and the level corresponding to the Type-C(2) configuration is at 0.74 eV below the CBM. As for the HSE06 results and for the Type-C(1) configuration, the defect level is found to be 1.38 eV below the CBM. The obtained positions of the levels in the gap for the bond-type C configurations indicate that these are not close enough to the CBM to be clearly considered shallow donor levels.

The defect levels belonging to the negatively charged systems are similarly positioned in the gap with respect to the levels of the same geometrical configurations of the neutral structures (Fig. 7).

In the case of the H^+ states (C configurations), no defect level is found in the gap. Due to the existence of a strong O-H bond the bonding state lies below the valence band and the antibonding state is positioned in the conduction band (see Fig. 7), in agreement with earlier calculations for hydrogen in oxides.[57]

The electronic charge densities for the defect levels were also evaluated for the three lowest-energy neutral systems as charge isosurfaces (shown in Fig. 8). For the Type-A and the Type-B configurations, which enable a defect level close to the valence-band maximum (Fig. 7), the isosurfaces are observed to possess an s-type state and the electron is localized at the hydrogen impurity. The contributions of the p-states that are depicted in Fig. 8 (upper and middle plots) around the impurity on the next-neighbor anions may be due to the close proximity of the defect level to the valence band, which is mainly of p-character (see Fig. 3). In contrast, in the Type-C neutral configuration the hydrogen electron is not localized at the impurity, but instead is centered at one of the closest cation neighbors (Fig. 8, bottom plot).

The displacement of the lattice in response to the impurity-anion bond, for the bond-type C configurations, causes significant changes in the elastic structural energies. These are related to a change of oxidation state of the corresponding anion (O^{2-} to OH^- state) causing the lengths of the neighboring bonds to adjust, thus resulting in large rearrangements of the host lattice.[59] Distortions of the octahedral coordination are therefore observed, since the bonded anion is driven away by about 0.34 Å from its original position, with respect to the neighbor cation. The displacement field and the hydrogen impurity causes the defect electron to be trapped close to the

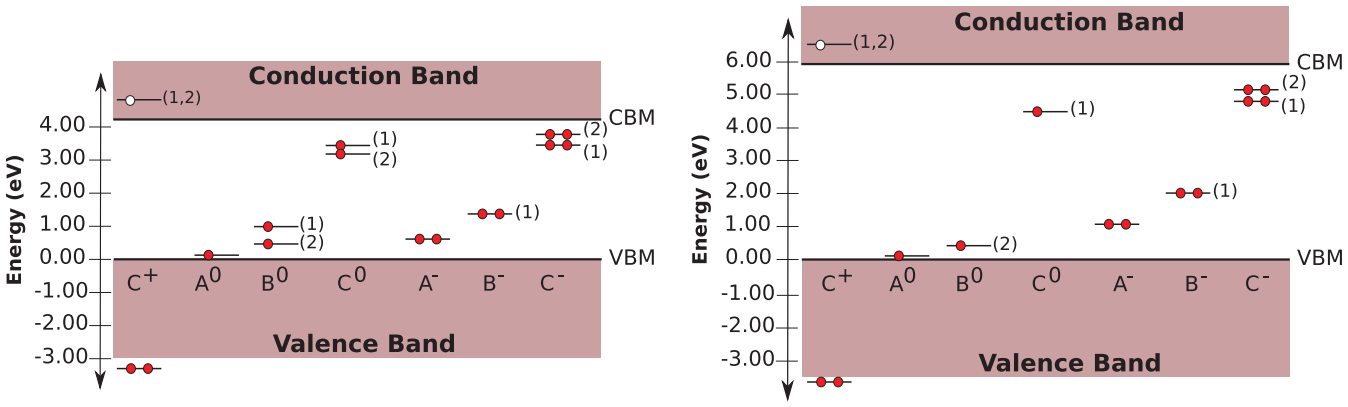

FIG. 7. (Color online) GGA-PBE (left) and HSE06 (right) defect levels (the respective occupations are represented by the red circles) of the three different charge states of the stable hydrogen configurations. The defect levels of the two different local environment of the Type-B and Type-C configurations, represented in Fig. 5, are denoted by (1) and (2). For the HSE06 calculations only the lowest-energy configurations are shown for the neutral charge systems. The energies are referenced from the VBM.

impurity atom, in which the singly occupied orbital is localized in a single metal cation.[18] These effects resemble the situation suggested by Cox *et al.*[18] for polaron formation where the defect centers may be either shallow or deep.

The alternative to the situation just described would be the competing tendency for the defect electron to delocalize.[59] If this was the case, the isosurfaces should evidence the delocalization of the charge densities of the defect electron throughout the lattice, suggesting that the impurity electron should be ionized to the conduction band due to the shallow-donor behavior of the hydrogen impurity. This hypothesis does not seem to be consistent with what is observed in the theoretical calculations: the defect level for the Type-C configuration not being close enough to the CBM to allow for a shallow-donor behavior (Fig. 7), the localized behavior observed from the isosurfaces plot (bottom plot of Fig. 8), and the lattice displacement observed for the structure of the Type-C configuration (as discussed in Sec. III A).

C. μSR results and discussion

We now discuss the assignment of the μSR components described in Sec. II B, which is most eased in the context of the calculations presented in the previous section. In order to address this question, we begin by presenting the temperature dependence of these components. Figure 9 displays the fractions f_{slow}, f_{fast}, and f_{Mu} of the slow, the fast, and the muonium (Mu) component, respectively, as a function of temperature between 15 K and 300 K. These have been obtained by comparison of the fitted asymmetries A_{slow}, A_{fast}, and A_{Mu} to the maximum instrumental asymmetry, as obtained from a calibration with silver. We note that the definition of the fast-relaxing muonium and fast components deteriorates for the highest values of relaxation, so that several fitting solutions are possible and the corresponding values of the fractions become affected by effective error bars larger than those represented in Fig. 9. Notwithstanding these uncertainties, the overall analysis has shown no appreciable temperature dependence of A_{Mu} with temperature, that corresponds to about 22.5% of the total muon polarization. The fraction of implanted muons ending up in this configuration is depicted in Fig. 9 (top) and thus corresponds to about $45 \pm 10\%$ of the total number of muons, since half of the polarization of the muons thermalizing as deep muonium is lost at low fields.[60] As shown in Fig. 9 (bottom), the slow diamagnetic component corresponds to $40 \pm 5\%$ at temperatures below 150 K and the data suggest an interconversion process to the fast component above this temperature. The sum of these two components adds to $51 \pm 10\%$ at all temperatures, so that the total fraction adds to $96 \pm 10\%$, suggesting that these three components account for the full muon polarization. This supports our assumption that the fast component has a diamagnetic character: if it corresponded to a heavily damped muonium line similar to what has been observed in α-TeO_2,[24] we would not expect to observe the full polarization. We have also undertaken a coarse transverse field dependence at 300 K, and verified that the diamagnetic model for the third component provides the best overall analysis. The corresponding relaxations λ_{slow} and λ_{fast} are represented as a function of temperature in Fig. 10 and Fig. 11, respectively.

These components of the μSR data can now be assigned to the hydrogen configurations found in the calculations, which indicate the lowest-energy configuration for the neutral state to be the Type-A configuration. In the calculations, this corresponds to a compact atomic state such as the muonium state observed experimentally. Furthermore, the calculations also confirm the acceptor-like character of this configuration. In fact, when calculating the isosurfaces regarding the negatively charged system of the lowest-energy configuration (Fig. 12) we obtain the same form of electron localization around the impurity (localization of two defect electrons). This can evidence the stability of the Type-A configuration with an additional electron added to the system. The Type-A configuration thus provides a most natural assignment for this experimentally observed state, which totals $\sim$45% of all muons at all temperatures.

At the lowest temperatures in our experiments, almost all remaining muons end up in the slowly relaxing diamagnetic state. We assign these to muons thermalizing as Mu^+. In principle, muon spectroscopy does not allow to distinguish Mu^+

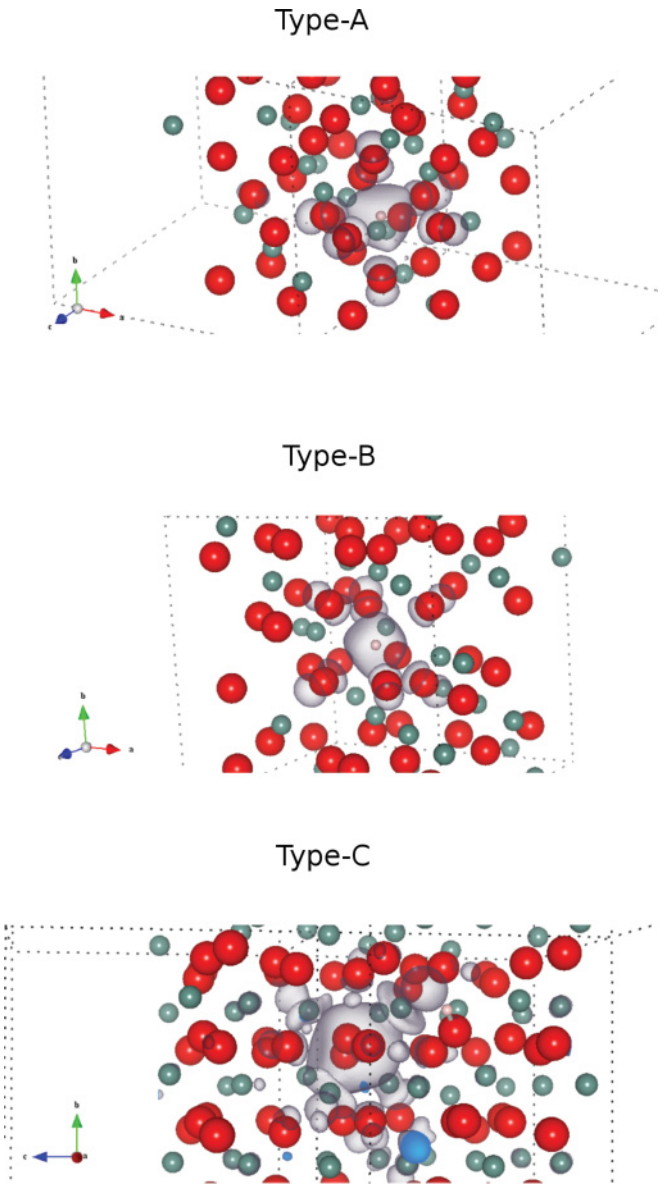

FIG. 8. (Color online) Isosurfaces of the electron charge densities for the defect level of the H^0 configurations. The Type-B and Type-C configurations refer to the lower-energy geometrical configurations. The calculations were carried out using the HSE06 functionals. The atoms are represented by their ionic radius, where O is depicted in red, Y in blue, and hydrogen in pink.

from Mu^-, both corresponding to the same diamagnetic frequency. However, Mu^- would eventually stabilize to the same position as Mu^0: as we will discuss below, the interconversion process between the slow and the fast components suggests that the muons ending in the slow-relaxing component jump to the Mu^0 position at higher temperatures. The assignment of the slow component to Mu^+ implies, taking into account the result of the calculations, that these muons stop at the Type-C configuration, which is the only stable site for H^+ and can host the donor hydrogen configurations. As shown in Fig. 10, the relaxation λ_{slow} of this component presents a remarkable decrease with increasing temperature, stabilizing at a small value of $\lambda_{slow} \sim 0.04\,\mu s^{-1}$ for temperatures above

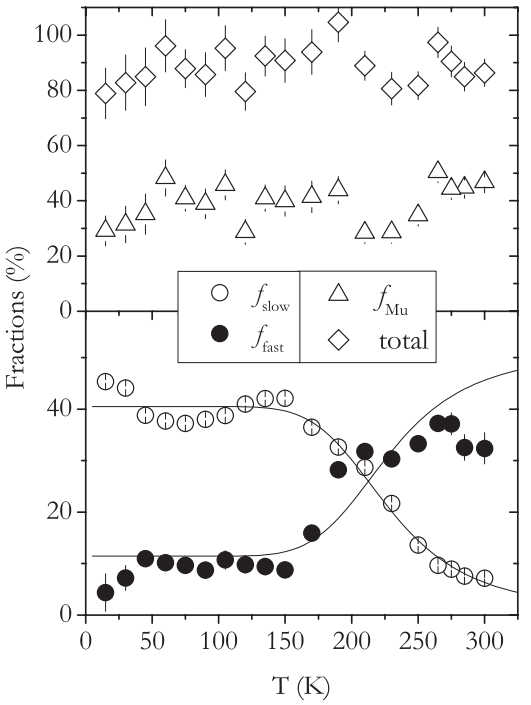

FIG. 9. Temperature dependence of the fraction of the different components observed in the μSR experiments. The slow and fast components are represented in the bottom, and lines are fits of a Boltzmann partition as discussed in the text. In the top, the muonium component and the total fraction are represented.

100 K. This is consistent with the behavior observed by Cox *et al.*,[18] the slightly higher value of relaxation in this work arising probably from a higher concentration of defects.[61–63] Using the atom positions calculated in this work, we estimate the relaxation expected for muons at the Type-C site, due to the nuclear dipolar broadening arising from the nearest ^{89}Y, to be around only $0.01\,\mu s^{-1}$ (despite the 100% abundance,

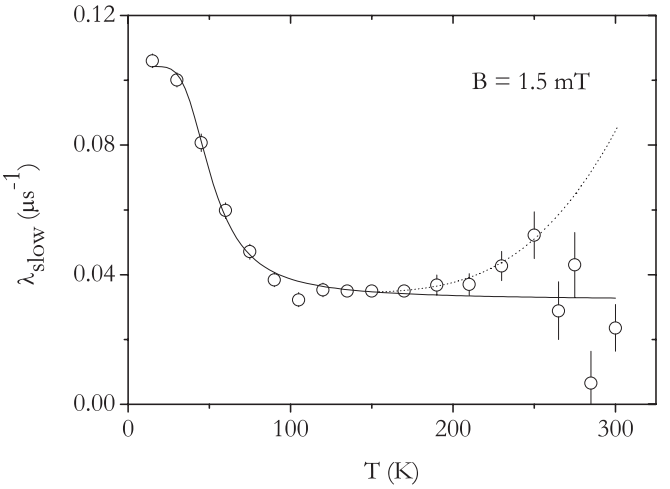

FIG. 10. Temperature dependence of the relaxation of the slow component. Line is a fit with the model described in Ref. 24, yielding an activation energy of 21(9) meV. The dashed line is a fit of an Arrhenius increase to the relaxation above 150 K, fixing an activation energy of 142 meV, as discussed in the text.

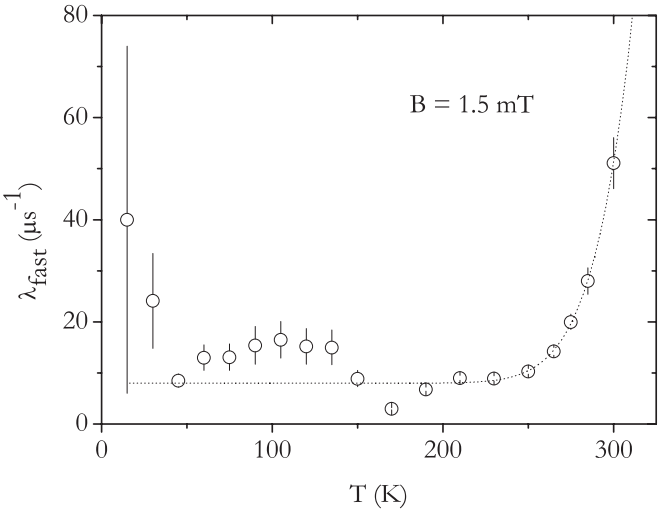

FIG. 11. Temperature dependence of the relaxation of the fast component. The dashed line is a fit of an Arrhenius increase to the relaxation above 150 K, yielding an activation energy of 372(16) meV, as discussed in the text.

the nuclear dipole moment of ^{89}Y nuclei is relatively low). This indicates that the relaxation values observed an order of magnitude higher at the lowest temperatures have an electronic origin. This relaxation has been interpreted in Refs. 18 and 24 as being due to the unresolved splitting of a shallow muonium center with an activation energy of 7(2) meV. Using the same model as in Ref. 24, we now extract a similar activation energy of 21(9) meV, consistent with the shallow-donor model. However, as discussed in Sec. III B, our calculations indicate donor transition levels $E(+/0)$, associated to the Type-C configurations, of 0.25 to 0.40 eV from the conduction-band minimum, an order of magnitude larger than the experimental value. These values are affected by an error bar which originates from the image corrections associated to the finite size of the supercell calculations and to the numerical convergence parameters adopted. The combined error can total 0.2 eV, so that the discrepancy between the experimental donor level and the theoretical donor level loses significance. As discussed in Sec. III B, the calculations suggest a polaronic model with the electron centered at the next cation and not at the impurity, which therefore appears an alternative candidate in order to justify the relaxation of the slow diamagnetic component. A shallow polaronic model has been considered before as an alternative to the hydrogenic shallow-donor model for oxides.[18]

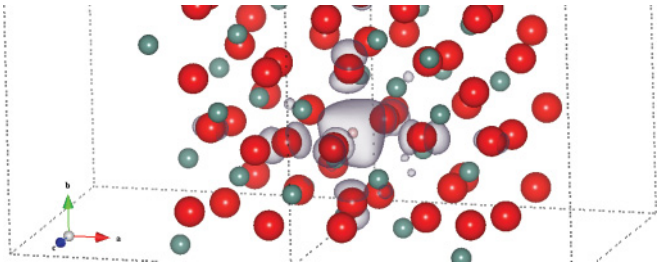

FIG. 12. (Color online) Isosurfaces of the electron charge densities for the defect level of the lowest-energy H^- configuration at the Type-A geometrical configuration. The calculations were carried out using the HSE06 functional. The atoms are represented by their ionic radius, where O is depicted in red, Y in blue, and hydrogen in pink.

We now discuss the assignment of the fast-relaxing component. Our fits suggest that this is a heavily relaxed diamagnetic component, which is present at a residual level for temperatures below 150 K and that becomes gradually more prominent as the slow component decreases above this temperature. We have thus assumed a phenomenological Boltzmann partition between these two components

$$f_{\rm slow}(T) = f_{\rm s0}\frac{1}{1+N\exp\left(-E_{\rm a}/k_{\rm B}T\right)}, \tag{4}$$

$$f_{\rm fast}(T) = f_{\rm s0}\frac{N\exp\left(-E_{\rm a}/k_{\rm B}T\right)}{1+N\exp\left(-E_{\rm a}/k_{\rm B}T\right)} + f_{\rm f0}, \tag{5}$$

where f_{s0} and f_{f0} are the total formation probabilities of the slow diamagnetic and the fast configurations, respectively, and $f_{s0} + f_{f0} = 0.51$. E_a is the activation energy of the process, k_B is the Boltzmann constant, and the empirical parameter N relates to the density of states. The simultaneous fit of Eqs. (4) and (5) to the data is represented in Fig. 9 (full lines), yielding $f_{s0} = 40(1)\%$, $f_{f0} = 11(2)\%$, $N = 1.3(6) \times 10^3$, and an activation energy $E_a = 142(10)$ meV. A possible process for this transition is the site change of Mu^+ from the donor-like Type-C configuration to the acceptor-like Type-A configuration, accompanied by the capture of an electron, in the combined process

$$\begin{aligned} {\rm Mu}_C{}^+ &\rightarrow {\rm Mu}_A{}^+ \\ {\rm Mu}_A{}^+ + e^- &\rightarrow {\rm Mu}_A{}^0. \end{aligned} \tag{6}$$

In this interpretation, the energy $E_a = 142$ meV corresponds to the activation energy for the site change process. This is suggested in Fig. 10, where the dashed line represents an Arrhenius-like fit to the relaxation of the slow component, above $T = 150$ K, fixing an activation energy of 142 meV. In this fit, the relaxation values above $T = 250$ K were ignored, since the corresponding fraction is too small to allow a precise determination of the relaxation. The relaxation of the fast component also presents a remarkable increase for temperatures above 200 K, which in this interpretation can be assigned to the charge capture process proposed to occur after the site change. A similar fit of an Arrhenius increase to the data above 150 K yields an activation energy of 371(16) meV to this process.

IV. CONCLUSION

Ab initio calculations and μSR spectroscopy measurements were carried out to characterize the nature of isolated hydrogen states in yttria. From the *ab initio* calculations it became possible to infer the existence of three stable configurations for the neutral and negatively charged systems. Two of these configurations are obtained when the hydrogen impurity stabilizes at the structural vacant O and Y interstitial sites (denoted as Type-A and Type-B configurations), whereas the third configuration is bond type where a covalent O-H bond is formed (denoted as Type-C configuration). The positively charged state was only found to adopt the latter Type-C configuration. The μSR experimental results directly reveal

the presence of two distinct muonium configurations, proposed to correspond to the Type-A acceptor-like configuration and to the Type-C donor-like configuration. Despite the metastability observed at low temperatures, the μSR results strongly suggest that at temperatures near room temperature all muons end up in the stable Type-A configuration, which thus appears quite robust.

The calculated formation energies obtained by both the semilocal and hybrid functionals place the hydrogen pinning level, $E(+/-)$, deep in the band gap, suggesting therefore an amphoteric behavior for hydrogen. The calculated acceptor levels are governed by the Type-A interstitial configurations and are consistent with earlier μSR data that inferred an acceptor level near midgap. The bond-type C configurations provide a range of donor levels within 0.25 eV (GGA-PBE) and 0.4 eV (HSE06) from the CBM overestimating the present μSR findings that place the donor level at 21(9) meV from the CBM.

The defect levels of the neutral and negatively charged systems lie close to the VBM, although for the Type-C structures this evidence is not observed. For the latter, the corresponding defect levels are positioned close to the CBM, although not close enough to allow a shallow-donor behavior of hydrogen. From the calculation of the isosurfaces for the Type-A and Type-B structures it was observed that the impurity electron is strongly localized at the hydrogen, hence indicating that these interstitial hydrogen configurations are deep, localized states. Concerning the Type-C configurations, the defect charge density is centered on a neighboring cation, which may suggest a lattice polaronic effect.

ACKNOWLEDGMENTS

The work was supported by the Program COMPETE: FCOMP-01-0124-FEDER-010450 and by the Portuguese Fundação para a Ciência e a Tecnologia (FCT) under Ciência 2007 and PTDC/FIS/102722/2008 research projects, and under the COMPETE: PEst-C/FIS/UI0036/2011 strategic project. The authors would also like to thank the computing support from the Department of Physics and the Milipeia cluster at the Laboratory for Advanced Computing of the University of Coimbra. Acknowledgments are also to be made to Fernando Nogueira and to the Condensed Matter Group of the Center for Computational Physics for fruitful discussions. The support of the muon teams at ISIS and PSI is also gratefully acknowledged.

*elora@teor.fis.uc.pt

†Also at: Escola Superior de Tecnologia da Saúde de Coimbra, Polytechnic Institute of Coimbra, P-3040-854 Coimbra, Portugal.

[1] G.-M. Rignanese, J. Phys.: Condens. Matter **17**, R357 (2005).

[2] J. X. Zheng, G. Ceder, T. Maxisch, W. K. Chim, and W. K. Choi, Phys. Rev. B **73**, 104101 (2006).

[3] J. Robertson, Rep. Prog. Phys. **69**, 327 (2006).

[4] P. W. Peacock and J. Robertson, J. Appl. Phys. **92**, 4712 (2002).

[5] W. C. Wang, M. Badylevich, V. V. Afana'ev, A. Stesmans, C. Adelmann, S. Van Elshocht, J. A. Kittl, M. Lukosius, Ch. Walczyk, and Ch. Wenger, Appl. Phys. Lett. **95**, 132903 (2009).

[6] J. X. Zheng and W. K. Chim, Phys. Status Solidi (RRL) **2**, 227 (2008).

[7] K. Xiong, J. Robertson, S. J. Clark, and S. J. Clark, in *Defects in High-K Gate Dielectric Stacks*, edited by E. Gusev, Vol. 220 (Springer, The Netherlands, 2006), p. 175.

[8] C. G. Van de Walle, Phys. Rev. Lett. **85**, 1012 (2000).

[9] C. G. Van de Walle and J. Neugebauer, Annu. Rev. Mater. Res. **36**, 179 (2006).

[10] J. M. Kahn, R. E. McMurray, E. E. Haller, and L. M. Falicov, Phys. Rev. B **36**, 8001 (1987).

[11] L. Tsetseris, D. M. Fleetwood, R. D. Schrimpf, and S. T. Pantelides, in *Defects in Microelectronic Materials and Devices*, edited by Daniel M. Fleetwood and Ronald D. Schrimpf (CRC Press Taylor & Francis Group, Boca Raton, 2009), Ch. 13, p. 381.

[12] C. G. Van de Walle and J. Neugebauer, Nature (London) **423**, 626 (2003).

[13] C. G. Van de Walle, P. J. H. Denteneer, Y. Bar-Yam, and S. T. Pantelides, Phys. Rev. B **39**, 10791 (1989).

[14] T. Norby and P. Kofstad, Solid State Ionics **20**, 169 (1986).

[15] T. Norby and P. Kofstad, J. Am. Ceram. Soc. **69**, 784 (1986).

[16] K. Xiong and J. Robertson, J. Appl. Phys. **102**, 083710 (2007).

[17] R. L. Lichti, K. H. Chow, and S. F. J. Cox, Phys. Rev. Lett. **101**, 136403 (2008).

[18] S. F. J. Cox, J. L. Gavartin, J. S. Lord, S. P. Cottrell, J. M. Gil, H. V. Alberto, J. P. Duarte, R. C. Vilão, N. A. de Campos, D. J. Keeble, E. A. Davis, M. Charlton, and D. P. van der Werf, J. Phys.: Condens. Matter **18**, 1079 (2006).

[19] K. H. Chow, B. Hitti, and R. F. Kiefl, in *Identification of Defects in Semiconductors*, edited by M. Stavola, Semiconductors and Semimetals, Vol. 51A (Academic Press, San Diego, 1998), p. 137, treatise edited by R. K. Willardson and E. R. Weber.

[20] S. F. J. Cox, J. S. Lord, S. P. Cottrell, J. M. Gil, H. V. Alberto, A. Keren, D. Prabhakaran, R. Scheuermann, and A. Stoykov, J. Phys.: Condens. Matter **18**, 1061 (2006), and included references therein.

[21] R. L. Lichti, K. H. Chow, J. M. Gil, D. L. Stripe, R. C. Vilão, and S. F. J. Cox, Physica B **376–377**, 587 (2006).

[22] R. C. Vilão, J. M. Gil, A. Weidinger, H. V. Alberto, J. Piroto Duarte, N. Ayres de Campos, R. L. Lichti, K. H. Chow, S. P. Cottrell, and S. F. J. Cox, Phys. Rev. B **77**, 235212 (2008).

[23] J. M. Gil, H. V. Alberto, R. C. Vilão, J. Piroto Duarte, N. Ayres de Campos, A. Weidinger, J. Krauser, E. A. Davis, S. P. Cottrell, and S. F. J. Cox, Phys. Rev. B **64**, 075205 (2001).

[24] R. C. Vilão, A. G. Marinopoulos, R. B. L. Vieira, A. Weidinger, H. V. Alberto, J. P. Duarte, and J. M. Gil, J. S. Lord, and S. F. J. Cox, Phys. Rev. B **84**, 045201 (2011).

[25] P. D. C. King, R. L. Lichti, Y. G. Celebi, J. M. Gil, R. C. Vilão, H. V. Alberto, J. Piroto Duarte, D. J. Payne, R. G. Egdell, I. McKenzie, C. F. McConville, S. F. J. Cox, and T. D. Veal, Phys. Rev. B **80**, 081201(R) (2009).

[26] J. M. Gil, H. V. Alberto, R. C. Vilão, J. Piroto Duarte, N. Ayres de Campos, A. Weidinger, E. A. Davis, and S. F. J. Cox, J. Phys.: Condens. Matter **13**, L613 (2001).

[27] S. Park, B. Lee, S. H. Jeon, and S. Han, Current Applied Physics **11**, S337 (2011).

[28] R. M. Nieminen, Model. Simul. Mater. Sc. Eng. **17**, 084001 (2009).

[29]J. Heyd, G. E. Scuseria, and M. Ernzerhof, J. Chem. Phys. **118**, 8207 (2003).
[30]A. Stroppa and S. Picozzi, Phys. Chem. Chem. Phys. **12**, 5405 (2010).
[31]A. Stroppa and G. Kresse, New J. Phys. **10**, 063020 (2008).
[32]A. Stroppa and G. Kresse, Phys. Rev. B **79**, 201201(R) (2009).
[33]A. Stroppa, K. Termentzidis, J. Paier, G. Kresse, and J. Hafner, Phys. Rev. B **76**, 195440 (2007).
[34]M. Marsman, J. Paier, A. Stroppa, and G. Kresse, J. Phys.: Condens. Matter **20**, 064201 (2008).
[35]A. Stroppa, M. Marsman, G. Kresse, and S. Picozzi, New J. Phys. **12**, 093026 (2010).
[36]H. Wu, A. Stroppa, S. Sakong, S. Picozzi, M. Scheffler, and P. Kratzer, Phys. Rev. Lett. **105**, 267203 (2010).
[37]A. Stroppa, G. Kresse, and A. Continenza, Phys. Rev. B **83**, 085201 (2011).
[38]R. Wyckoff, *Crystal Structures* (Wiley, New York, 1963), Vol. 1.
[39]F. Jollet, C. Noguera, N. Thromat, M. Gautier, and J. P. Duraud, Phys. Rev. B **42**, 7587 (1990).
[40]H. Yusa, T. Tsuchiya, N. Sata, and Y. Ohishi, Inorg. Chem. **49**, 4478 (2010).
[41]P. Villars and L. D. Calvert, *Pearson's Handbook of Crystallographic Data for Intermetallic Phases*, 2nd Ed. (ASM International, Ohio, 1991), Vol. IV.
[42]Y.-N. Xu, Z. Q. Gu, and W. Y. Ching, Phys. Rev. B **56**, 14993 (1997).
[43]J. P. Perdew, K. Burke, and M. Ernzerhof, Phys. Rev. Lett. **77**, 3865 (1996); **78**, 1396(E) (1997).
[44]G. Kresse and J. Furthmüller, Phys. Rev. B **54**, 11169 (1996).
[45]G. Kresse and J. Hafner, Phys. Rev. B **47**, R558 (1993).
[46]G. Kresse and J. Furthmüller, Comput. Mat. Sci. **6**, 15 (1996).
[47]G. Kresse and D. Joubert, Phys. Rev. B **59**, 1758 (1999).
[48]P. E. Blöchl, Phys. Rev. B **50**, 17953 (1994).
[49]H. J. Monkhorst and J. D. Pack, Phys. Rev. B **13**, 5188 (1976).
[50]O. Ünal and M. Akinc, J. Am. Ceram. Soc. **79**, 805 (1996).
[51]B. Xu, V. R. Cooper, D. J. Singh, and Y. P. Feng, Phys. Rev. B **83**, 064115 (2011).
[52]L. Ning, Y. Zhang, and Z. Cui, J. Phys.: Condens. Matter **21**, 455601 (2009).
[53]L. Marsella and V. Fiorentini, Phys. Rev. B **69**, 172103 (2004).
[54]C. G. Van de Walle, Physica B: Condens. Matter **376–377**, 1 (2006).
[55]C. G. Van de Walle and J. Neugebauer, J. Appl. Phys. **95**, 3851 (2004).
[56]C. G. Van de Walle, in *Electron Devices Meeting, 2005* (IEDM Technical Digest. IEEE International, 2005), p. 403.
[57]J. Robertson and P. W. Peacock, Thin Solid Films **445**, 155 (2003).
[58]P. W. Peacock and J. Robertson, Appl. Phys. Lett. **83**, 2025 (2003).
[59]P. A. Cox, in *Transition Metal Oxides* (Clarendon Press, Oxford, 1992), ch. 2.
[60]B. D. Patterson, Rev. Mod. Phys. **60**, 69 (1988).
[61]J. M. Gil, P. J. Mendes, L. P. Ferreira, H. V. Alberto, R. C. Vilão, N. Ayres de Campos, A. Weidinger, Y. Tomm, Ch. Niedermayer, M. V. Yakushev, R. D. Tomlinson, S. P. Cottrell, and S. F. J. Cox, Phys. Rev. B **59**, 1912 (1999).
[62]R. C. Vilão, J. M. Gil, H. V. Alberto, J. Piroto Duarte, N. Ayres de Campos, A. Weidinger, M. V. Yakushev, and S. F. J. Cox, Physica B **326**, 181 (2003).
[63]V. Corregidor, D. Martín y Marero, J. M. Gil, and E. Díeguez, Europhys. Lett. **67**, 247 (2004).